

## Multi-Mode Heat Transfer Simulations of the Onset and Propagation of Thermal Runaway in a Pack of Cylindrical Li-Ion Cells

To cite this article: Dhananjay Mishra and Ankur Jain 2021 *J. Electrochem. Soc.* **168** 020504

View the [article online](#) for updates and enhancements.

### Discover the EL-CELL potentiostats


- Fully independent test channels with Pstat / GStat / EIS
- Optionally with integrated temperature controlled cell chamber
- Unique Connection Matrix: Switch between full-cell and half-cell control at runtime

[www.el-cell.com](http://www.el-cell.com) +49 (0) 40 79012 734 [sales@el-cell.com](mailto:sales@el-cell.com)





# Multi-Mode Heat Transfer Simulations of the Onset and Propagation of Thermal Runaway in a Pack of Cylindrical Li-Ion Cells

Dhananjay Mishra and Ankur Jain<sup>z</sup> 

Mechanical and Aerospace Engineering Department, University of Texas at Arlington, Arlington, Texas, United States of America

Strategies to prevent or minimize propagation of thermal runaway in a pack of Li-ion cells are critically needed to ensure safe operation, storage and transportation. While significant literature already exists on thermal runaway simulations, several key questions of practical relevance have remained unaddressed. This work presents multi-mode heat transfer simulations to predict the onset and propagation of thermal runaway in a pack of cylindrical Li-ion cells. The impact of inter-cell gap and thermal properties of the interstitial material on onset and propagation of thermal runaway is studied. It is shown that high interstitial thermal conductivity promotes thermal runaway propagation. However, too low a thermal conductivity results in heat localization in the trigger cell, also leading to thermal runaway. An optimum range of interstitial material thermal conductivity is thus identified. The impact of trigger cell position on propagation is investigated. It is shown that, depending on external conditions, either the center or the corner position may be more susceptible to propagation. Finally, it is shown that radiation and natural convection play a key role in thermal runaway propagation. It is expected that the trade-offs identified here will help minimize the onset and propagation of thermal runaway in Li-ion battery packs.

© 2021 The Electrochemical Society ("ECS"). Published on behalf of ECS by IOP Publishing Limited. [DOI: 10.1149/1945-7111/abcd7b]

Manuscript submitted November 12, 2020; revised manuscript received December 22, 2020. Published February 1, 2021.

## List of Symbols

$b$	hemispherical reflectivity
$C_p$	specific heat capacity ( $\text{Jkg}^{-1} \text{K}^{-1}$ )
$f$	shape factor
$\mathbf{g}$	acceleration due to gravity vector ( $\text{ms}^{-2}$ )
$k$	thermal conductivity ( $\text{Wm}^{-1} \text{K}^{-1}$ )
$L$	length of the box (m)
$p$	pressure ( $\text{Nm}^{-2}$ )
$q''$	heat flux ( $\text{Wm}^{-2}$ )
$q'''$	volumetric heat generation rate ( $\text{Wm}^{-3}$ )
$R_u$	universal gas constant ( $\text{JKg}^{-1} \text{K}^{-1}$ )
$T$	temperature (K)
$\mathbf{V}$	velocity vector ( $\text{m s}^{-1}$ )
$w$	distance between wall and cylinder (m)
$W$	width of the box (m)
$\alpha$	thermal diffusivity ( $\text{m}^2 \text{s}^{-1}$ )
$\beta$	volumetric thermal expansion coefficient ( $\text{K}^{-1}$ )
$\varepsilon$	hemispherical emissivity
$\rho$	density ( $\text{kg m}^{-3}$ )
$\sigma$	Stefan-Boltzmann constant ( $\text{Wm}^{-2} \text{K}^{-4}$ )
$\mu$	dynamic viscosity ( $\text{kg m}^{-1} \text{s}^{-1}$ )
$r, \theta, z$	Cylindrical coordinates
$x, y, z$	Cartesian coordinates

Li-ion cells are used universally for energy conversion and storage in a wide variety of engineering applications.<sup>1</sup> Li-ion cells offer high power density, long cycle life and low self-discharge rate.<sup>2</sup> However, temperature sensitivity of Li-ion cells remains a key technological challenge.<sup>3,4</sup> When subjected to thermal, mechanical or electrical abuse, such as high temperature, nail penetration or overcharging, Li-ion cells undergo a series of exothermic decomposition reactions, leading to an unsustainable cycle of heat generation and temperature rise, often referred to as Thermal Runaway (TR).<sup>5,6</sup> Thermal runaway presents serious safety and reliability concerns during the operation, storage and transportation of Li-ion cells. The cell and the battery pack must both be designed to prevent the onset and propagation of thermal runaway.

Thermal runaway is known to comprise a series of exothermic decomposition processes, wherein each process generates the heat needed to trigger the next process. Key thermal runaway processes in a Li-ion cell include SEI decomposition, negative and positive electrode decomposition reaction and electrolyte decomposition reaction.<sup>5</sup> Each of these reactions are known to be governed by Arrhenius reaction kinetics, which has been comprehensively studied by experimental and theoretical methods.<sup>5,6</sup>

Thermal modeling and simulations are critical for understanding and mitigating thermal runaway in practical systems, because experimental measurements of thermal runaway in a large battery pack are hazardous, expensive and time-consuming.<sup>7</sup> Due to the non-linear nature of thermal runaway, only a limited number of analytical heat transfer solutions for thermal runaway exist, including a non-dimensional number to predict the onset of thermal runaway,<sup>8</sup> non-dimensional analysis of heat transfer during thermal runaway,<sup>9</sup> and semi-analytical thermal modeling of temperature distribution during thermal runaway in realistic conditions.<sup>10</sup> Most of such work is limited to analysis of a single cell, which does not provide sufficient insights into thermal phenomena that may occur when a number of cells are packed together for operation, transportation or storage.

In contrast to the limited literature on analytical methods, a wide variety of thermal simulation studies have been presented in the literature. The inherent non-linearity of thermal runaway poses challenges in thermal simulations, particularly when thermal behavior of a large number of cells in a pack is to be studied. A three-dimensional lumped thermal abuse model has been developed to predict the spatial distribution of temperature within a battery pack.<sup>11</sup> This work showed that the cell size plays a key role in thermal runaway propagation. Quantitative strategies to prevent thermal runaway propagation in a large format battery pack have been developed using a combination of lumped method simulations and experimental measurements.<sup>12</sup> Cascading propagation of thermal runaway in a battery pack has been studied, showing that pouch cells may be more susceptible than cylindrical cells due to larger area of contact.<sup>13</sup> Statistical distribution of energy released during thermal runaway—an important input parameter for simulations—has been studied.<sup>14</sup> A simulations-based study of the impact of tab configurations, vent locations and intercellular gaps on thermal runaway propagation has been presented.<sup>15</sup> In another study highlighting the importance of electrical connectivity and cell form

<sup>z</sup>E-mail: jaina@uta.edu

factor, pouch cells were found to propagate more rapidly than cylindrical cells due to greater contact area, and cells connected in parallel showed greater propagation than cells in series.<sup>13</sup> This work also demonstrated the importance of thermal conductivity in deciding the thermal fate of the battery pack. Based on Accelerated Rate Calorimetry and Gaussian approximation curve, a comprehensive numerical model to estimate thermal abuse tolerance of a battery pack has been proposed.<sup>16,17</sup> A finite-element based electro-thermal runaway model for Lithium Titanate battery pack has been developed for studying the nature of thermal runaway propagation in the pack.<sup>18</sup>

Several papers have also investigated various strategies to mitigate the propagation of thermal runaway. A passive strategy for mitigating propagation based on reduction in state of charge and use of metal plates between cells to enhance thermal transport has been presented.<sup>19</sup> A similar mitigation technique by inserting physical barriers of different thermal properties between cells has also been presented.<sup>18</sup> Dividing a large number of cells in a battery pack into smaller groups using thermal barriers has been investigated.<sup>20</sup> A numerical investigation of the extent of thermal runaway mitigation using phase change materials and metal plates around the cell has been presented.<sup>21</sup> An active thermal runaway mitigation system based on conduits and breaches evenly distributed throughout battery pack has also been proposed.<sup>22</sup> Liquid cooling of prismatic cell pack has been shown to prevent thermal runaway.<sup>23</sup>

Propagation of thermal runaway in a battery pack, or a group of cells packed together for transportation/storage is likely to be influenced by how the cells are arranged in the pack, properties of the interstitial material and the location of the trigger cell. However, despite the comprehensive literature on thermal simulations on Li-ion battery pack in general, there is a lack of robust simulation models that account for all three modes of heat transfer—conduction, convection and radiation—and predict the impact of such parameters on thermal runaway onset and propagation. The impact of thermal conductivity of the material between cells in a range of thermal abuse conditions has not been sufficiently described. Finally, the impact of the location of the trigger cell in the pack on thermal runaway propagation is also unclear.

This paper presents a multimodal, non-linear, three-dimensional thermal transport simulation of thermal runaway onset and propagation in an array of cylindrical cells. The simulations account for all three modes of heat transfer between cells, as well as the non-linear Arrhenius kinetics representing multiple exothermic decomposition reactions. The unique contributions of the present work, relative to past literature, include the identification of an optimum range of thermal conductivity of the interstitial material, within which, the risk of both onset and propagation of thermal runaway is lowered. Further, the present work helps understand the impact of the location of trigger cell within the battery pack. The importance of accounting for radiation and natural convection in thermal runaway propagation simulations is also highlighted. This work helps understand the complicated, non-linear interactions between various transport phenomena responsible for the propagation of thermal runaway. This work is expected to be of interest to the battery community since the results obtained here provide practical guidelines for ensuring safety during operation, transportation and storage of Li-ion battery packs.

### Simulation Setup

**Geometry.**—The simulation geometry is shown schematically in Fig. 1a. Finite-volume simulations are carried out on a 5 by 5 array of 18650 cells surrounded by an interstitial material with a uniform gap between cells. A 1 mm thick heater is wrapped around one of the cells, referred to as the trigger cell. Joule heating in the heater triggers thermal runaway. The entire array of cells is placed inside a box, with 2.5 mm clearance between the cells and the box. The simulations account for temperature-dependent heat generation due

to decomposition reactions coupled with thermal conduction through all materials, natural convection in the air around the cells, as well as cell-to-cell heat transfer due to radiation. Several of these processes are highly non-linear. In contrast to prismatic cells, where a one-dimensional simulation is often possible, the cylindrical geometry of cells considered here necessitates a three-dimensional simulation. The governing equations for each of these phenomena are described below in detail.

**Governing equations.—Heat generation.**—Heat generation due to four specific decomposition reactions are considered—SEI decomposition, negative-solvent reaction, positive-solvent reaction and electrolyte decomposition. Arrhenius expressions for heat generation for each reaction are assumed, as listed in Table I.<sup>24</sup> These expressions account for reactant consumption as the reaction proceeds. Values for various parameters appearing in the heat generation equations are taken from Kim, et al.<sup>11</sup> and listed in Table II. Joule heating in the 1 mm thick heater around the trigger cell due to heating current is modeled as a volumetric heat source.

**Thermal conduction.**—Amongst the three modes of heat transfer, thermal conduction is relatively the easiest to model. The transient energy equation governing thermal conduction in each cylindrical cell is given by

$$\frac{k_r}{r} \frac{\partial}{\partial r} \left( r \frac{\partial T}{\partial r} \right) + \frac{k_\theta}{r^2} \frac{\partial^2 T}{\partial \theta^2} + k_z \frac{\partial^2 T}{\partial z^2} + q''' = \rho c_p \frac{\partial T}{\partial t} \quad [1]$$

Thermal conductivity of the cell is taken to be orthotropic due to the rolled nature of the cell. Similarly, thermal conduction in the interstitial material outside each cell is governed by the following equation in the Cartesian coordinate system

$$k \frac{\partial}{\partial x} \left( \frac{\partial T}{\partial x} \right) + k \frac{\partial}{\partial y} \left( \frac{\partial T}{\partial y} \right) + k \frac{\partial}{\partial z} \left( \frac{\partial T}{\partial z} \right) + q''' = \rho c_p \frac{\partial T}{\partial t} \quad [2]$$

Unlike the Li-ion cell, thermal conductivity of the interstitial material is taken to be isotropic.

**Natural convection.**—Due to the large temperature rise expected on cell surfaces because of thermal runaway, buoyancy-driven natural convection heat transfer may be important to model, even though the time scale for natural convection is probably much larger than the time scale available during thermal runaway. Natural convection is modeled by turning on gravitational effects and implementing a temperature-dependent density of air, which results in convective flow driven by the temperature difference between hot surfaces and the ambient. Convection is, of course, not relevant if the interstitial material between cells is solid. The conservation equations governing convective flow and heat transfer due to natural convection is

$$\nabla \cdot (\rho \mathbf{V}) = 0 \quad [3]$$

$$\rho \left( \frac{\partial \mathbf{V}}{\partial t} + (\mathbf{V} \cdot \nabla) \mathbf{V} \right) = -\nabla \cdot \mathbf{p} + \mu \nabla^2 \mathbf{V} + \rho \mathbf{g} \beta (T - T_\infty) \quad [4]$$

$$\mathbf{V} \cdot \nabla T = \alpha \nabla^2 T \quad [5]$$

where viscous effects are neglected in the energy equation due to low velocity of air. Note that the  $\mathbf{g} \cdot \beta (T - T_\infty)$  term in Eq. 4 drives natural convection due to change in density with temperature. Here,  $\beta$  is the volumetric thermal expansion coefficient, which quantifies the rate at which the density of air changes with temperature at constant pressure. By treating air to be an ideal gas,  $\beta$  can be shown to be given by<sup>25</sup>

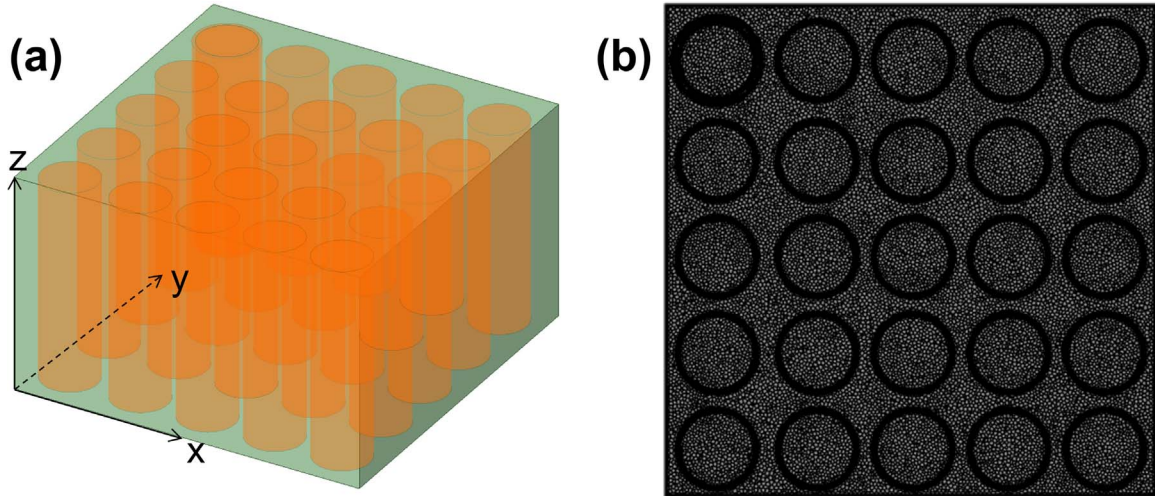


**Figure 1.** Schematic of 18650 Li-ion battery pack containing 25 cells: (a) Geometry of battery pack with trigger cell at position 1 and intercellular gap of 4 mm. (b) Cross sectional view of the 3D tetrahedral meshing elements used in the simulation.

**Table I. Governing Equations and parameters for heat generation rates of various processes responsible for thermal runaway.**<sup>24</sup>

Reaction	Heat Generation	Rate of Reaction
SEI decomposition	$Q_{sei} = H_{sei} \cdot W_c \cdot R_{sei}$	$R_{sei} = A_{sei} \cdot \exp\left[\frac{-Ea_{sei}}{RuT}\right] \cdot C_{sei}^m$ ; $\frac{dC_{sei}}{dt} = -R_{sei}$
Negative -solvent reaction	$Q_{ne} = H_{ne} \cdot W_c \cdot R_{ne}$	$R_{ne} = A_{ne} \cdot \left[\frac{-tsei}{tsei, ref}\right] \cdot \exp\left[\frac{-Ea_{ne}}{RuT}\right] \cdot C_{ne}^m$ ; $\frac{dC_{ne}}{dt} = -R_{ne}$
Positive-solvent reaction	$Q_{pe} = H_{pe} \cdot W_p \cdot R_{pe}$	$R_{pe} = A_{pe} \cdot \alpha^{m,pe} \cdot (1-\alpha)^{m,pe} \cdot \exp\left[\frac{-Ea_{pe}}{RuT}\right]$ ; $\frac{d\alpha}{dt} = R_{pe}$
Electrolyte decomposition	$Q_e = H_e \cdot W_e \cdot R_e$	$R_e = A_e \cdot \exp\left[\frac{-Ea_e}{RuT}\right] \cdot C_e^m$ ; $\frac{dC_e}{dt} = -R_e$

$$\beta = -\frac{1}{\rho} \frac{\Delta\rho}{\Delta T} = \frac{1}{\rho} \frac{p}{R_u T^2} = \frac{1}{T} \quad [6]$$

**Radiation.**—Similar to natural convection, radiative heat transfer between cells may be an important heat transfer mode due to the large temperature rise expected in the battery pack when thermal runaway occurs. Implementation of radiative heat transfer in the simulation is carried out using the surface-to-surface radiation model in ANSYS Fluent. In this model, radiation exchange between any pair of surfaces within the simulation geometry is governed by the view factor, which accounts for the sizes, separation distance and relative orientation of the two surfaces.

The energy flux leaving a surface is composed of emitted energy by virtue of temperature and reflected energy, which is dependent on irradiation flux from surroundings. For any surface  $i$ , the amount of energy leaving the surface is<sup>26</sup>

$$q_{out,i} = \varepsilon_i \sigma T_i^4 + b_i q_{in,i} \quad [7]$$

where  $\varepsilon_i$  and  $b_i$  are the emissivity and reflectivity, respectively, of the  $i^{\text{th}}$  surface, and  $\sigma$  is the Boltzmann constant.  $q_{in,i}$  is the irradiation

flux incident on the surface from the surroundings, which is given by the net sum of energy incident from all other surfaces based on the view factors  $f_{ji}$  as follows:

$$A_i \cdot q_{in,i} = \sum_N^{j=1} A_j \cdot q_{out,j} \cdot f_{ji} \quad [8]$$

Therefore, Eq. 7 can be re-written as

$$q_{out,i} = \varepsilon_i \cdot \sigma T_i^4 + b_i \cdot \sum_N^{j=1} f_{ij} \cdot q_{out,j} \quad [9]$$

Thus, total radiation flux from a surface comprises of Stefan-Boltzmann emission from the surface and sum of the radiation fluxes intercepted and reflected by virtue of other surfaces in the visible surroundings. This radiation flux is included as a heat input term for each cell in computing the energy equation.

View factors play a key role in the radiative heat transfer modeling approach used in this work, and are calculated for each face pair in the geometry using ray tracing method.<sup>27</sup> In this method, a large number of rays are fired from points on a given object at various angles, and the first object that each ray intersects is

**Table II. Physical and kinetic parameters used for abuse simulations.<sup>11</sup>**

Symbol	Description	Value
$A_{sei}$	SEI-decomposition frequency factor	$1.667 \times 10^{15} \text{ (s}^{-1}\text{)}$
$A_{ne}$	Negative-solvent frequency factor	$2.5 \times 10^{13} \text{ (s}^{-1}\text{)}$
$A_{pe}$	Positive-solvent frequency factor	$6.667 \times 10^{13} \text{ (s}^{-1}\text{)}$
$A_e$	Electrolyte decomposition frequency factor	$5.14 \times 10^{25} \text{ (s}^{-1}\text{)}$
$Ea_{sei}$	SEI-decomposition activation energy	$1.3508 \times 10^5 \text{ (Jmol}^{-1}\text{)}$
$Ea_{ne}$	Negative-solvent activation energy	$13508 \times 10^5 \text{ (Jmol}^{-1}\text{)}$
$Ea_{pe}$	Positive-solvent activation energy	$1396 \times 10^5 \text{ (Jmol}^{-1}\text{)}$
$Ea_e$	Electrolyte-decomposition activation energy	$2.74 \times 10^5 \text{ (Jmol}^{-1}\text{)}$
$C_{sei0}$	Initial value of $C_{sei}$	0.15
$C_{ne0}$	Initial value of $C_{ne}$	0.75
$\alpha_0$	Initial value of $\alpha$	0.04
$C_{e0}$	Initial value of $C_e$	1
$m_{sei}$	Reaction order for $C_{sei}$	1
$m_{ne}$	Reaction order for $C_{ne}$	1
$m_{pe,p1}$	Reaction order for $\alpha$	1
$m_{pe,p2}$	Reaction order for $(1-\alpha)$	1
$m_e$	Reaction order for $C_e$	1
$t_{sei,ref}$	Initial value of $t_{sei}$	0.033
$H_{sei}$	Sei-decomposition heat release	$257 \text{ (Jg}^{-1}\text{)}$
$H_{ne}$	Negative-solvent heat release	$1714 \text{ (Jg}^{-1}\text{)}$
$H_{pe}$	Positive-solvent heat release	$314 \text{ (Jg}^{-1}\text{)}$
$H_e$	Electrolyte decomposition heat release	$155 \text{ (Jg}^{-1}\text{)}$
$W_c$	Specific Carbon content	$6.104 \times 10^5 \text{ (gm}^{-3}\text{)}$
$W_p$	Specific positive active material content	$1.221 \times 10^6 \text{ (gm}^{-3}\text{)}$
$W_e$	Specific Electrolyte content	$4.069 \times 10^5 \text{ (gm}^{-3}\text{)}$

recorded. The view factor between any two objects is then computed as the fraction of rays leaving the first object and intersecting the second.

For the purposes of simulation of radiative heat transfer, all surfaces in the simulation geometry are considered to be gray and diffuse, with an emissivity of 0.1. The low value of emissivity is justified by the shiny, metallic surface finish of most Li-ion cells, resulting in high reflectivity and low emissivity.

**Meshing and other simulation details.**—3D polyhedral meshing is used for all simulations in this work due to high resolution and low meshing time compared to other meshing techniques. Surface meshing is carried out with local sizing of 1 cell per gap, scoped to faces, selected by labels and proximity size control type. Volume

meshing comprises polyhedral elements with 1.2 growth rate, 30° mesh feature angle and 0.9 quality warning limit. Upwards of 10 Million elements are used in the mesh for the 25-cell geometry, with a maximum orthogonal quality of 0.43. The squish index of the meshing, which characterizes polyhedral mesh quality is 0.31. A solver with fixed time advancement technique with 0.001 s step size and 500 maximum iterations per time step is used with total simulation time being 1000 s. A representative cross-section showing the mesh is presented in Fig. 1b. A comprehensive mesh sensitivity analysis is carried out prior to actual simulations in order to determine the minimum spatial discretization and time step needed to obtain grid-independent results. This analysis is carried out by refining the spatial meshing or time step, one at a time, until the results do not change significantly with further refinement. Relative tolerance for each iteration is set as 0.001. 500 energy iterations per timestep and 3000 faces per surface cluster are used.

Thermal conductivity of each cell is treated to be orthotropic, with values of  $0.2 \text{ Wm}^{-1} \text{ K}^{-1}$ ,  $32 \text{ Wm}^{-1} \text{ K}^{-1}$  and  $32 \text{ Wm}^{-1} \text{ K}^{-1}$  in the radial, axial and circumferential directions, respectively, based on past measurements.<sup>28</sup> Density and heat capacity are taken to be  $2280 \text{ kg m}^{-3}$  and  $715 \text{ J kg}^{-1} \text{ K}^{-1}$ ,<sup>24</sup> respectively, also based on past measurements.<sup>24,28</sup> The baseline interstitial material around cells is taken to be air, which is modeled as an incompressible ideal gas, with constant viscosity, specific heat and thermal conductivity. Variations in the thermal conductivity of the interstitial material are considered in simulations discussed in the next section.

## Results and Discussion

**Simulation validation.**—The simulation set up described in the previous Section is validated in multiple ways. Due to the complicated, non-linear nature of the simulation, several elements of the simulation, such as Arrhenius heat generation and radiative heat transfer are validated separately.

In order to validate the radiation modeling approach, a radiative heat transfer problem with a simpler but representative geometry is considered. As shown in the inset in Fig. 2, a single cylinder of

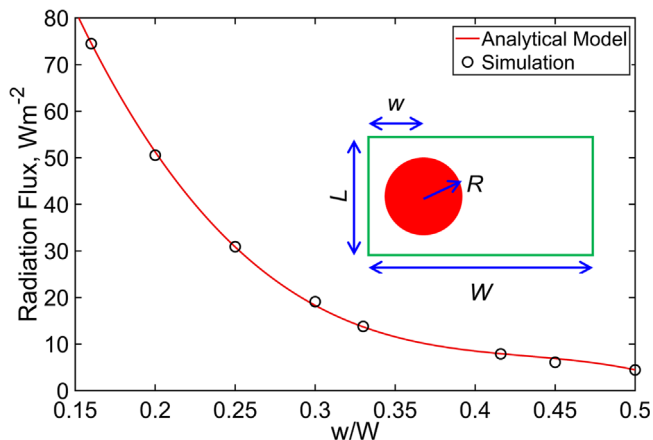


**Figure 2.** Validation of simulation results against analytical model for surface-to-surface radiation modeling: (a) Radiation flux intercepted by cell at 298 K temperature located inside a box from the left wall at 373 K temperature as a function of  $w/W$ . A geometrical schematic is shown as an inset.

radius  $R$  is located inside a rectangular box of size  $L$  by  $W$ . The distance between one of the walls and the center of the cylinder is  $w$ . For this simplified geometry, the radiative heat exchange between the left wall and cylinder is given by

$$q'_{\text{cyl-wall}} = \varepsilon \left[ \frac{2}{\pi} \tan^{-1} \left( \frac{L}{2w} \right) \right] \sigma (T_{\text{cyl}}^4 - T_{\text{wall}}^4) \quad [10]$$

where  $L$  is the length of wall and  $w$  is the distance between wall and cylinder. Figure 2 presents a comparison of the theoretical radiative heat transfer based on Eq. 10 and one computed using the view factor determined from the ray tracing method described in the previous Section. This comparison, presented as a function of  $w/W$  shows that as  $w/W$  increases, the radiative flux reduces, as expected, due to the greater distance between the cylinder and the wall. There is excellent agreement between the numerical calculation of the radiative heat flux and the theoretical curve throughout the  $w/W$  range. While the single-cylinder geometry used here for validation is fairly simple, it is reasonably representative of the geometry used in actual simulations while still allowing an analytical solution that the numerical calculations can be compared against.

Unlike radiation, a well-known theoretical solution is not readily available that can be compared with the simulation's computation of natural convection while still maintaining a geometry representative of a battery pack. Instead, the velocity field computed by the simulation is plotted in order to confirm that natural convection effects are indeed being accounted for by the simulation model. These velocity color plots are shown in Fig. 3 over a cross-section at three different times for a representative simulation. The left-most cell is the trigger cell, and the cell-to-cell gap is 4 mm. Velocity field is plotted only in the air outside the cells, since there is no convection inside the cells. Figure 3 clearly shows generation of a natural convection velocity field over time. Initially, the velocity field is generated in the gap next to the trigger cell due to the high temperature of the walls of the trigger cell. As time passes and thermal runaway takes place in the trigger cell, the cell walls become even hotter, which increases the driving force behind natural convection. This is clearly seen in Figs. 3b and 3c where the natural convection flow spreads out and even propagates downwards in the gap between other cells. Note that Fig. 3 plots the velocity magnitude, and not its direction.

For further validation of the computational approach used in this work, results from a single-cell simulation are compared with a semi-analytical model available from the literature.<sup>10</sup> For a single

cylindrical cell of 18650 configuration with convective cooling on the outer surface, a semi-analytical model based on discrete time stepping and the use of a closed-form temperature solution in each timestep has been presented in the past.<sup>10</sup> Four decomposition reactions are modeled in the cell in addition to a fixed Joule heating current for triggering thermal runaway. Under these conditions, numerical simulation is carried out to determine the temperature at the core of the cell as a function of time. Radiation and natural convection are switched off, since the semi-analytical model used for comparison does not account for these effects.<sup>10</sup> Figure 4 presents comparison of the numerical simulation with the semi-analytical model. Core temperature as a function of time is plotted in Fig. 4a, while reactant concentration parameters are plotted in Fig. 4b. In both cases, there is excellent agreement between the two. Temperature rises slowly at first while the cell is being heated up by Joule current before the exothermic decomposition reactions take over, resulting in very rapid temperature rise. Soon, however, the decomposition reactions fade away due to consumption of reactants, resulting in a gradual reduction in temperature seen in Fig. 4a. The consumption of reactants can be seen clearly in Fig. 4b. The good agreement between numerical simulation results and the semi-analytical model from past work, even though for a simplified geometry, provides further validation of the numerical simulation framework described in Section 2.

**Effect of cell gap on TR propagation.**—The effect of parameters external to the cell on thermal runaway propagation is investigated first. Two key parameters of specific interest are cell-to-cell gap and thermal conductivity of the interstitial material around the cells. Figure 5 presents colormaps of computed temperature distribution at three different times for two cases where the cell-to-cell gap is 4 mm and 1 mm, respectively. A plot of core temperature of the cells as functions of time is presented in Fig. 6. Recognizing the symmetry in the problem, temperatures of only cells in the right half of the geometry are plotted. For cell numbers used in Fig. 6, please refer to the numbering scheme shown in Fig. 5. In these simulations, the thermal conductivity of the interstitial material is held constant at  $k = 0.02 \text{ Wm}^{-1} \text{ K}^{-1}$  (roughly corresponding to air) and the trigger cell is located at a corner. A heating rate of  $4 \times 10^5 \text{ Wm}^{-2}$  up to 400 s is implemented in the sleeve heater around the trigger cell.

Figures 5 and 6 show two very different outcomes of the battery pack, depending on the value of the cell-to-cell gap. When the cell-to-cell gap is 1 mm, the small thermal resistance offered by the interstitial material results in sufficient heat transfer from the trigger

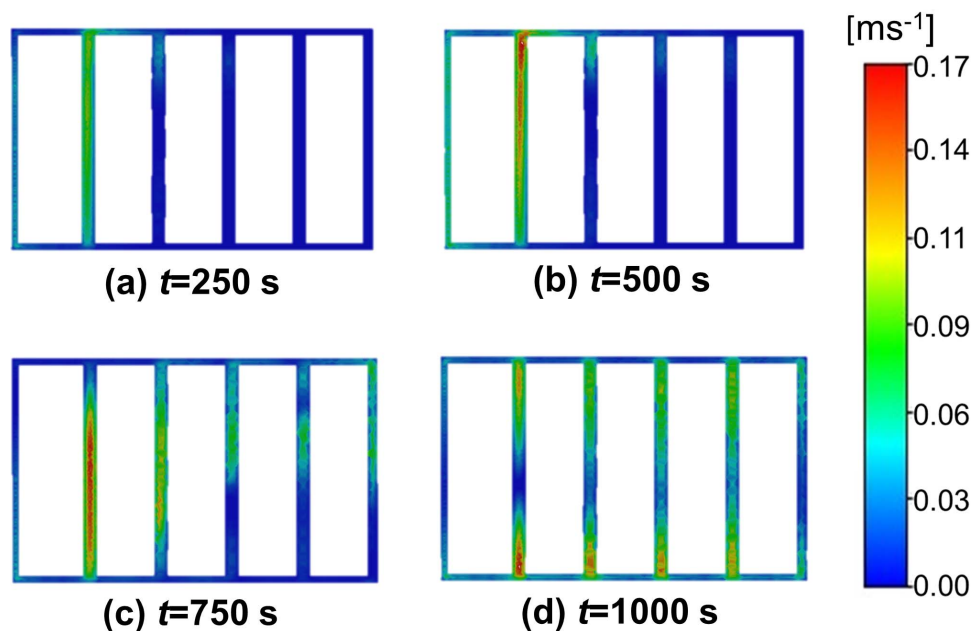


**Figure 3.** Velocity colormap at different time steps to demonstrate establishment of convective flow and heat transfer between cells as simulation progresses: (a) 250 s, (b) 500 s, (c) 750 s, (d) 1000 s. These colormaps are shown on a cross-section across five cells, where the left-most cell is the trigger cell and the cell-to-cell gap is 4 mm.

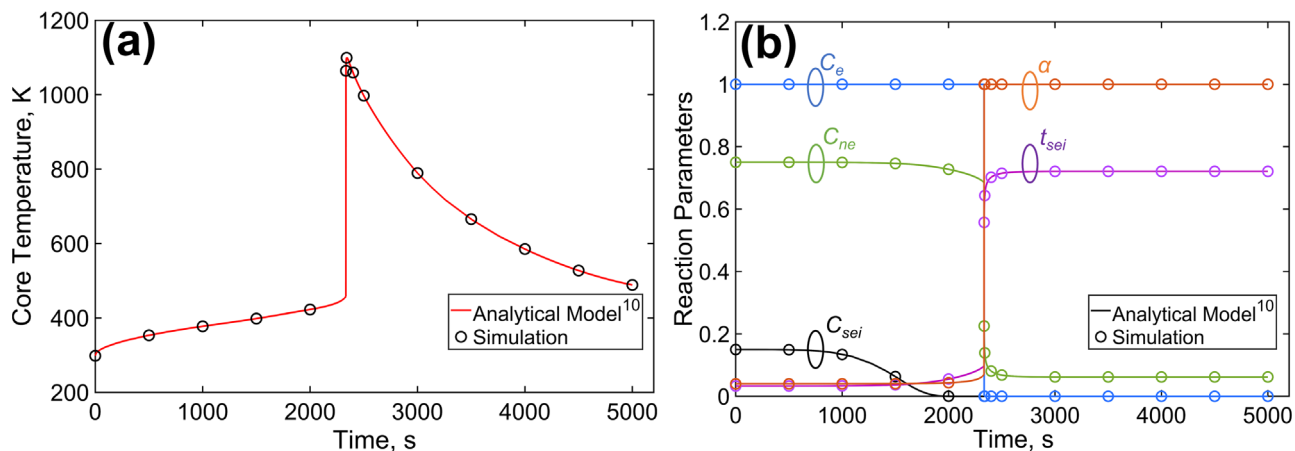


**Figure 4.** Validation of simulations against analytical model<sup>10</sup> for thermal runaway onset in response to convective heat transfer from a heater ambient maintained at 423 K: Plots of (a) temperature, and (b) various reactant concentration parameters as functions of time during a thermal runaway event.

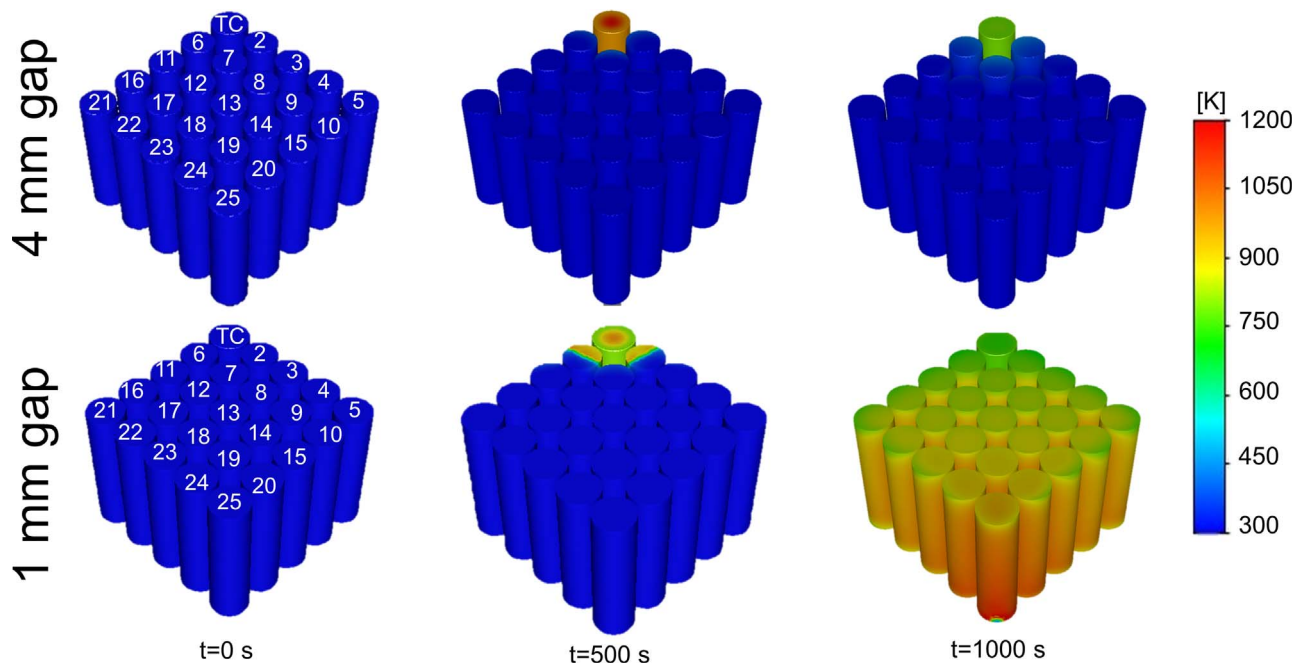


**Figure 5.** Effect of cell-to-cell gap on thermal runaway propagation: Temperature contours at three specific times during a thermal abuse event for two different values of the cell-to-cell gap. Thermal conductivity of the interstitial material is  $0.02 \text{ Wm}^{-1} \text{ K}^{-1}$  and heating rate is  $4 \times 10^5 \text{ Wm}^{-2}$  for 0–400 s.

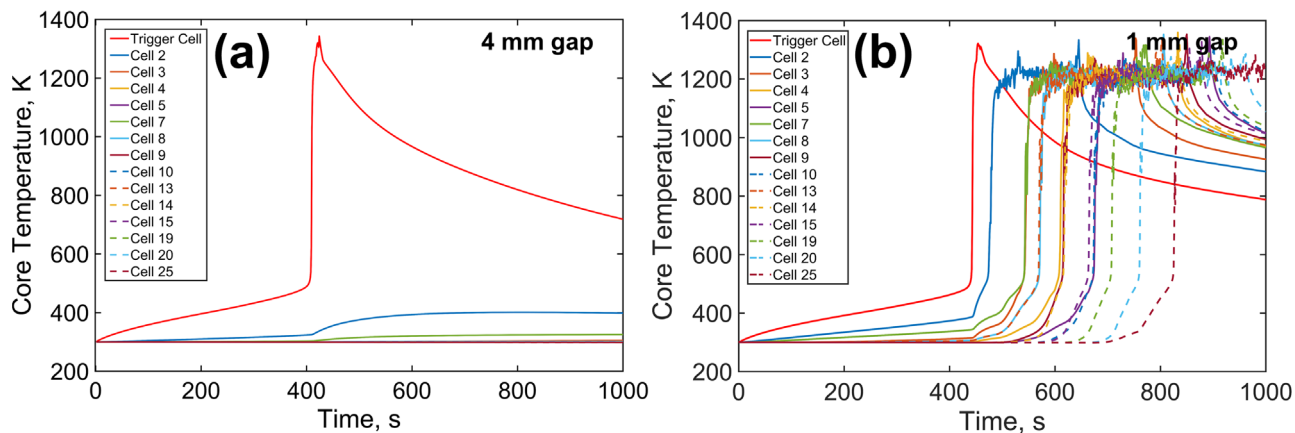
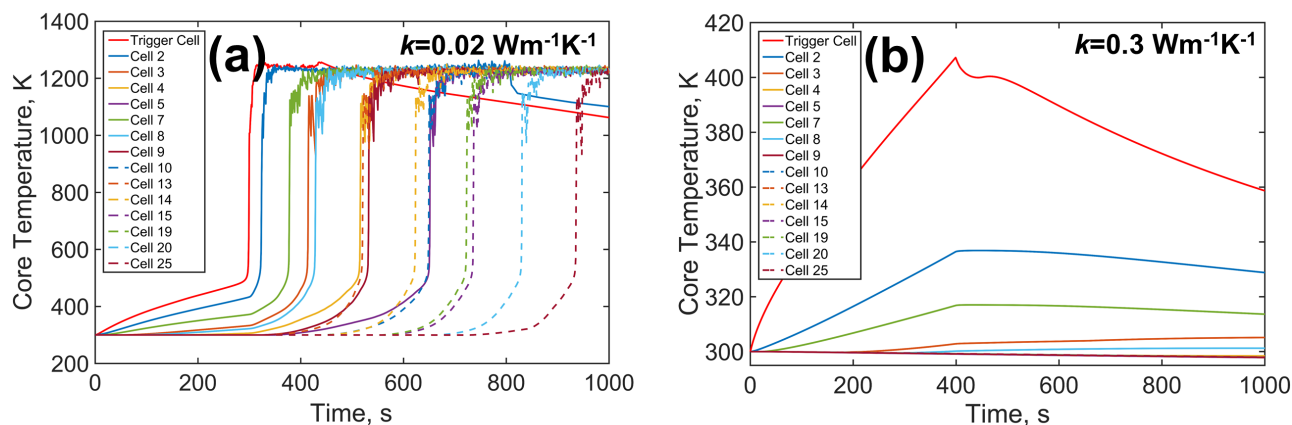


**Figure 6.** Temperature vs time plots for each cell for the scenario considered in Fig. 5 with cell-to-cell gap of (a) 4 mm, (b) 1 mm.

## Scenario 1



## Scenario 2

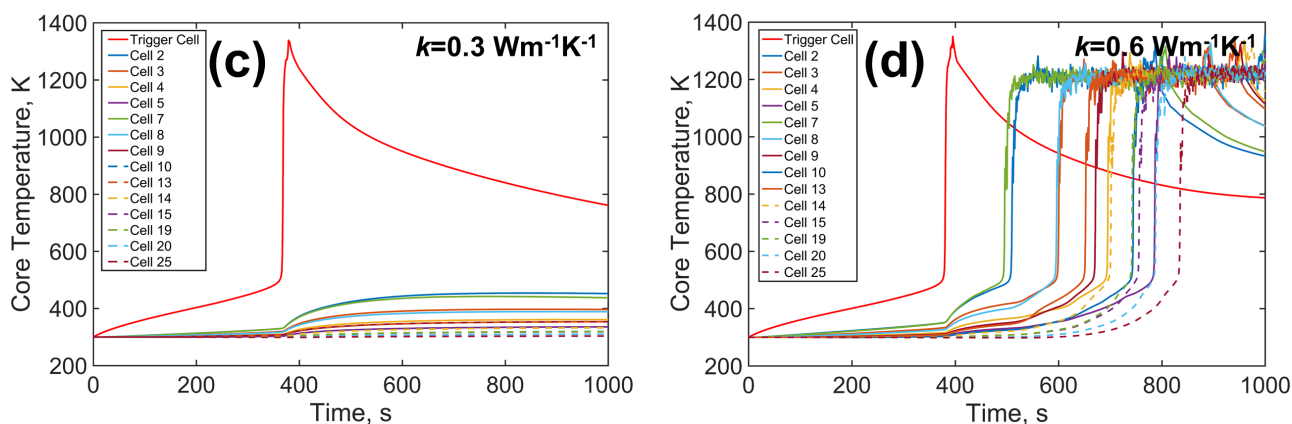


**Figure 7.** Temperature contours for investigating the effect of thermal conductivity of the interstitial material: (a) and (b) present plots for  $k = 0.02 \text{ Wm}^{-1} \text{ K}^{-1}$  and  $k = 0.3 \text{ Wm}^{-1} \text{ K}^{-1}$  under Scenario 1 (heating rate of  $4 \times 10^5 \text{ Wm}^{-2}$  for 0–400 s and external convective heat transfer coefficient of  $10 \text{ W/m}^2\text{K}$ ); (c) and (d) present plots for  $k = 0.3 \text{ Wm}^{-1} \text{ K}^{-1}$  and  $k = 0.6 \text{ Wm}^{-1} \text{ K}^{-1}$  under Scenario 2 (heating rate of  $5 \times 10^5 \text{ Wm}^{-2}$  for 0–400 s and external convective heat transfer coefficient of  $0 \text{ Wm}^{-2} \text{ K}^{-1}$ ).

cell to its neighbors to cause propagation of thermal runaway, first from the trigger cell to its neighbors and eventually into the entire battery pack. In contrast, a cell-to-cell gap of 4 mm offers large enough thermal resistance and suppression of heat transfer that propagation of thermal runaway does not occur, even though there is some temperature rise in the neighboring cells, as evident from Fig. 6a. Note that the tipping point in the cell-to-cell gap to prevent thermal runaway propagation, which lies between 1–4 mm in this case, depends on various problem parameters, including the thermal conductivity of the interstitial material ( $0.02 \text{ Wm}^{-1} \text{ K}^{-1}$  in this case), the cell size (18650 configuration in this case), the heat generation mechanisms for thermal runaway (standard, four-reaction model as summarized in Table I), etc. For other values of these parameters, the critical value of the cell-to-cell gap will vary and must be calculated separately.

Note that the thermal behavior seen in Figs. 5 and 6 represents fairly strong sensitivity of thermal runaway propagation on cell-to-cell gap. In practical scenarios of low-cost transportation and storage, it is quite possible that the cell-to-cell gap cannot be controlled to this degree of accuracy as ambient conditions around the cell change, for example, during air transportation of cells.

The effect of thermal conductivity of the interstitial medium is investigated next.

**Effect of thermal conductivity of interstitial material on TR propagation.**—In addition to the cell-to-cell gap, thermal conductivity

of the interstitial material also impacts thermal conduction from the trigger cell to its neighbors, and therefore, is expected to play a key role in thermal runaway propagation. High value of thermal conductivity may facilitate more heat transfer to neighboring cells, which may cool down the trigger cell, possibly helping to stop the onset of thermal runaway, but may also increase the heat absorbed by neighboring cell, causing propagation of thermal runaway. The opposite is true for low values of thermal conductivity—in this case, neighboring cells may remain thermally shielded from the trigger cell, but, low thermal conductivity also enhances the possibility of onset of thermal runaway by concentrating heat within the trigger cell. These arguments suggest that there may be an optimal window of thermal conductivity of the interstitial material, below or above which, there may be greater likelihood of thermal runaway onset and propagation.

A series of simulations are carried out on a 5 by 5 cell matrix in order to systematically investigate these issues. In these simulations, the cell-to-cell gap is held constant at 4 mm, and the trigger cell is always at the corner (Cell 1). Since the trigger cell may experience different amounts of thermal abuse in realistic conditions, two distinct scenarios are considered. In Scenario 1, a heating rate of  $4 \times 10^5 \text{ Wm}^{-2}$  up to 400 s is considered, along with a value of  $h = 10 \text{ Wm}^{-2} \text{ K}^{-1}$  for the external convective heat transfer coefficient. Within these parameters, simulations are carried out for two values of interstitial thermal conductivity— $0.02 \text{ Wm}^{-1} \text{ K}^{-1}$  and  $0.3 \text{ Wm}^{-1} \text{ K}^{-1}$ . Results are shown in Figs. 7a and 7b, respectively,



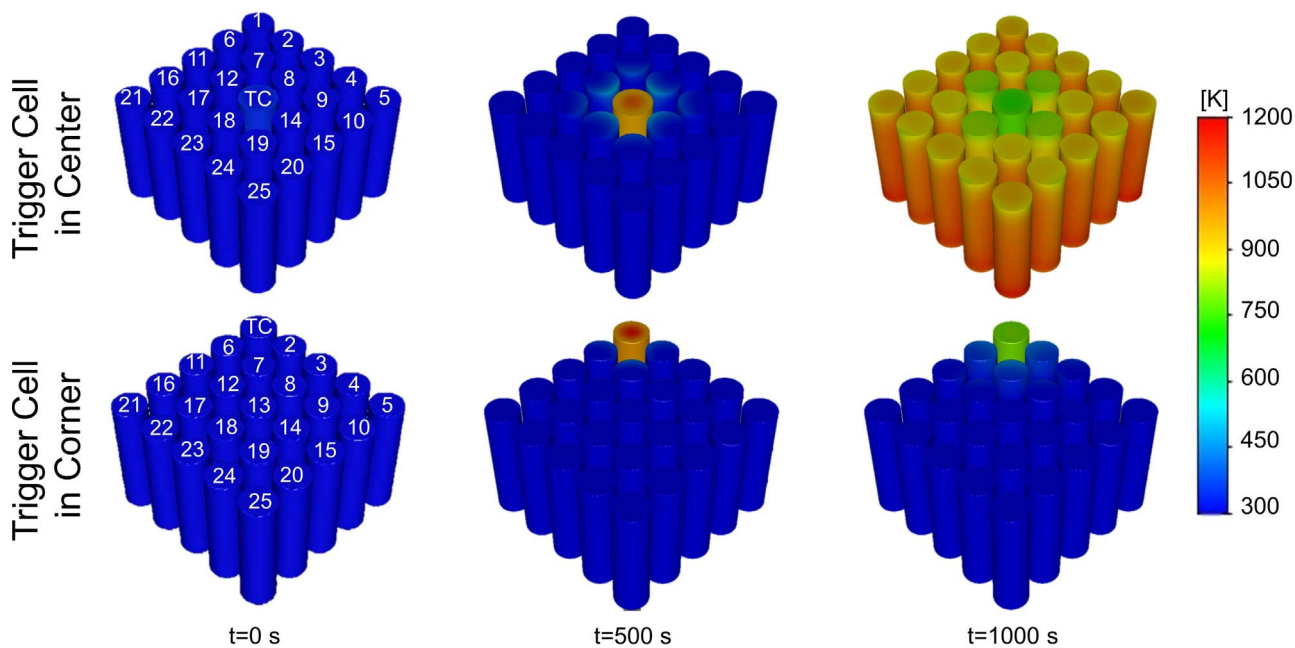


**Figure 8.** Effect of position of trigger cell on thermal runaway propagation in Scenario A (heating rate of  $4 \times 10^5 \text{ Wm}^{-2}$  for 0–400 s and external convective heat transfer coefficient of  $10 \text{ Wm}^{-2} \text{ K}^{-1}$ ): Temperature contours at three specific times for (a) Trigger cell at the center; (b) Trigger cell at the corner.

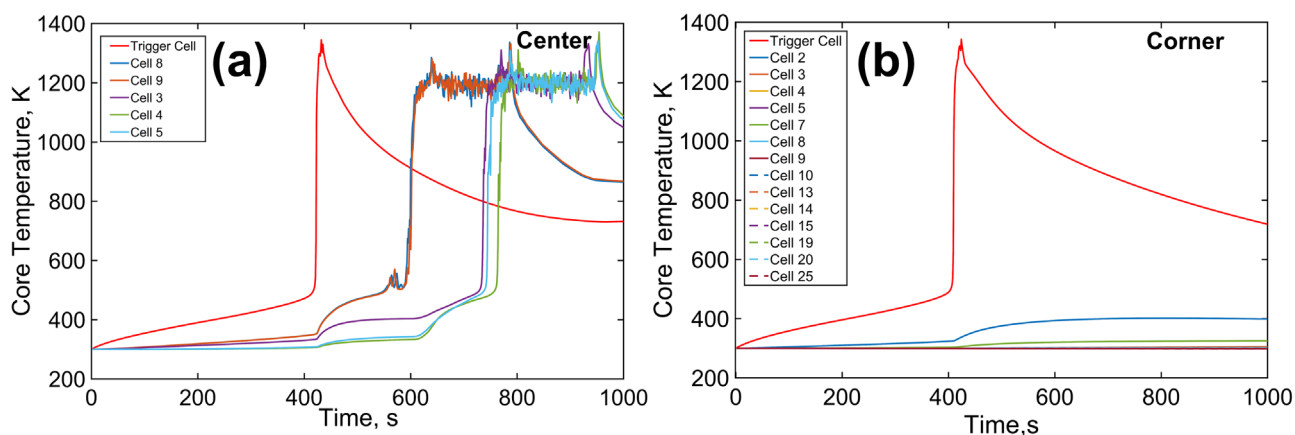


**Figure 9.** Temperature vs time plots for each cell for the scenario considered in Fig. 8 with (a) Trigger cell at the center; (b) Trigger cell at the corner.

in the form of peak temperatures of each cell plotted as functions of time. These results indicate that low thermal conductivity causes thermal localization within the trigger cell, leading to onset of thermal runaway in the trigger cell. Once thermal runaway is initiated, the large amount of heat generated causes propagation into neighboring cells. On the other hand, when the thermal conductivity is  $0.3 \text{ Wm}^{-1} \text{ K}^{-1}$ , there is greater heat spreading from the trigger cell. In this case, as shown in Fig. 7b, there is some temperature rise in the trigger cell as well as its neighbors, but not enough to cause thermal runaway. Therefore, under the abuse conditions of Scenario 1, a larger thermal conductivity is desirable. However, this may not be generalized to all possible abuse conditions. A second set of abuse conditions, Scenario 2 is considered, with  $5 \times 10^5 \text{ Wm}^{-2}$  heating up to 400 s, along with adiabatic boundary conditions on the outside of the battery pack. This represents a greater thermal abuse than Scenario 1. In this case, simulations are carried out for thermal conductivity values of  $0.3 \text{ Wm}^{-1} \text{ K}^{-1}$  and  $0.6 \text{ Wm}^{-1} \text{ K}^{-1}$ . The resulting temperature curves for cells in the pack are plotted in Figs. 7c and 7d, respectively. These results show a behavior that is opposite of Scenario 1. In this case, the lower value of thermal conductivity causes sufficient

reduction in thermal conduction that thermal runaway does not propagate, despite the trigger cell entering thermal runaway, as seen in Fig. 7c. At the higher value of thermal conductivity considered here, Fig. 7d shows that the increased thermal conduction in this case results in propagation of thermal runaway eventually into all cells of the battery pack.

These results indicate that a low value of thermal conductivity may be desirable for some thermal abuse conditions, but undesirable for others. An intermediate value of thermal conductivity, such as the  $0.3 \text{ Wm}^{-1} \text{ K}^{-1}$  case considered here, appears to present a reasonable balance by preventing propagation of thermal runaway in both scenarios considered here. Therefore, an intermediate value of thermal conductivity of the interstitial material is likely to be most effective in preventing propagation of thermal runaway across a range of abuse scenarios. This desirable, intermediate range of thermal conductivity may be specific to other conditions, such as cell-to-cell gap and cell chemistry, and therefore, may need to be determined specifically for each battery pack. Nevertheless, the existence of this optimal range of thermal conductivity, as demonstrated by simulations described above, is interesting and highlights the critical influence of thermal conductivity of the interstitial material on thermal runaway propagation.

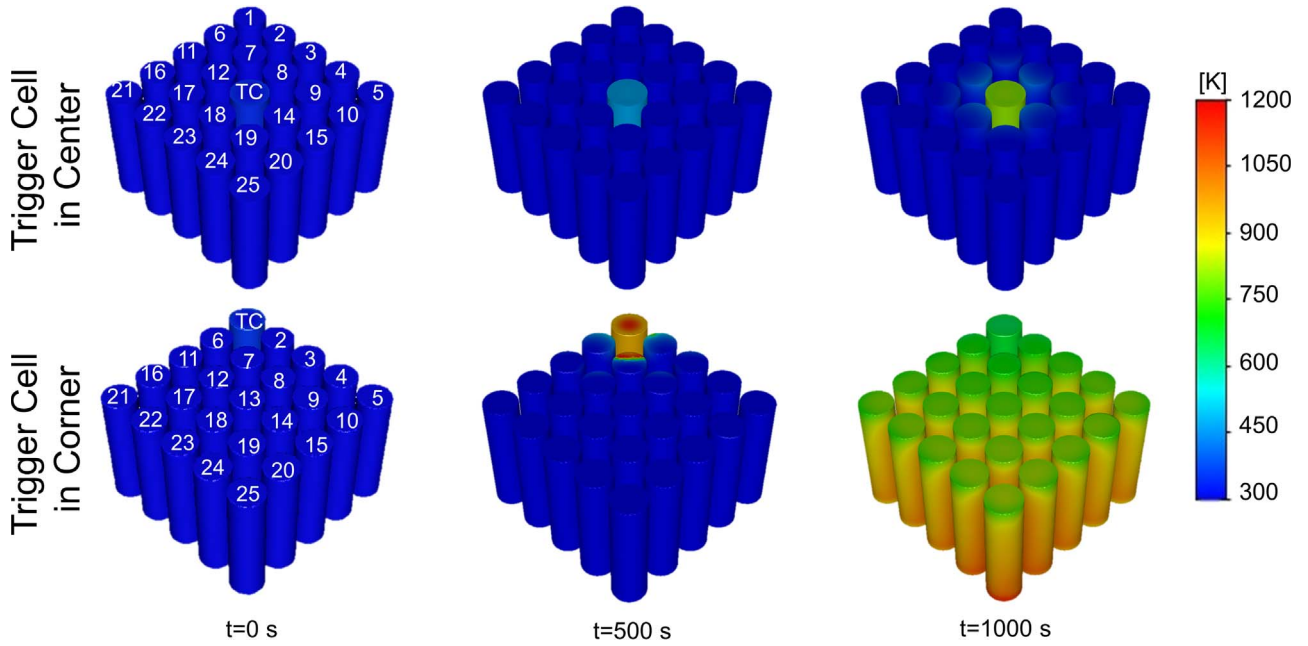


**Figure 10.** Effect of position of trigger cell on thermal runaway propagation in Scenario B (heating rate of  $3 \times 10^5 \text{ Wm}^{-2}$  for 0–400 s and external convective heat transfer coefficient of  $0 \text{ Wm}^{-2} \text{ K}^{-1}$ ): Temperature contours at three specific times for (a) Trigger cell at the center; (b) Trigger cell at the corner.

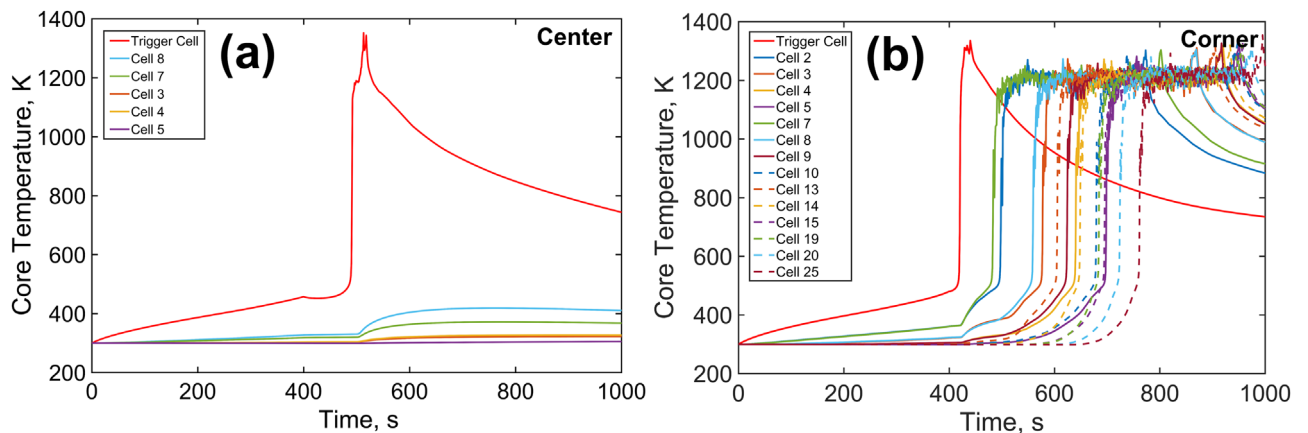


**Figure 11.** Temperature vs time plots for each cell for the scenario considered in Fig. 10 with (a) Trigger cell at the center; (b) Trigger cell at the corner.

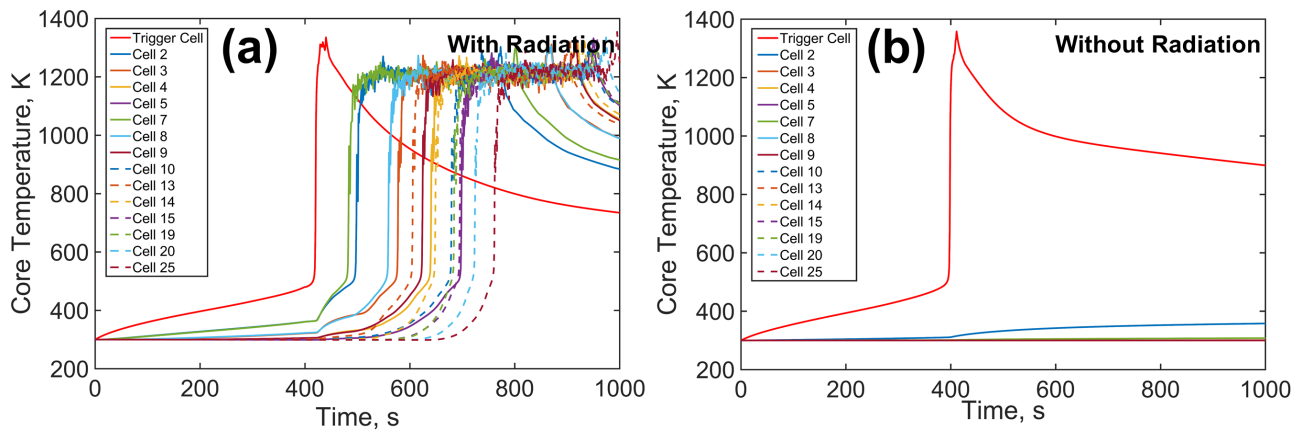


**Figure 12.** Impact of modeling of radiative heat transfer on the prediction of thermal runaway propagation: Temperature vs time plots for each cell in the pack (a) with radiation modeling, (b) without radiation modeling. In both cases, the cell-to-cell is 4 mm, thermal conductivity of interstitial material is  $0.02 \text{ Wm}^{-1} \text{ K}^{-1}$ , external convective heat transfer coefficient is  $0 \text{ Wm}^{-2} \text{ K}^{-1}$ , trigger cell is at center, and heating rate is  $3 \times 10^5 \text{ Wm}^{-2}$  for 0–400 s.

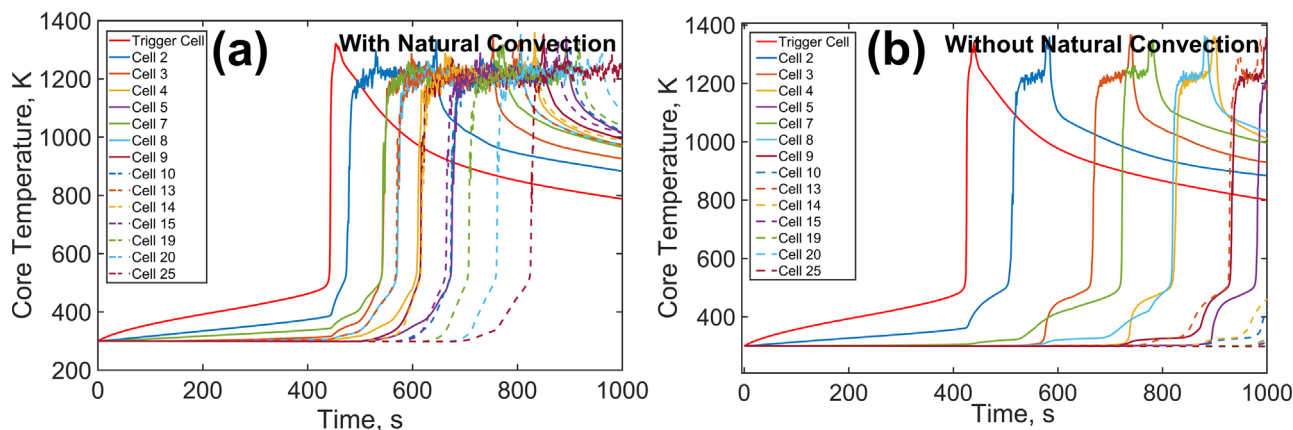


**Figure 13.** Effect of modeling of natural convection on the prediction of thermal runaway propagation: Temperature vs time plots for each cell in the pack (a) with natural convection modeling, (b) without natural convection modeling. In both cases, the cell-to-cell is 1 mm, thermal conductivity of interstitial material is  $0.02 \text{ Wm}^{-1} \text{ K}^{-1}$ , external convective heat transfer coefficient is  $10 \text{ Wm}^{-2} \text{ K}^{-1}$ , trigger cell is at a corner, and heating rate is  $4 \times 10^5 \text{ Wm}^{-2}$  for 0–400 s.

**Effect of trigger cell position on TR propagation.**—It is of interest to determine whether thermal runaway propagation is affected by the location of the trigger cell in the battery pack. Two competing considerations appear to be relevant for determining the impact of the trigger cell location. First, if the trigger cell is located at the corner or edge of the battery pack, then it has easier access to external cooling such as convection available on the boundary of the battery pack. In contrast, heat removal from a trigger cell located in the center is much more difficult, and most of the heat is likely to be distributed to the neighboring cells. However, the second consideration is that when located in the center, the trigger cell has more neighbors, and therefore, the heat gained by each neighbor may be lower, thereby lowering the risk of thermal runaway propagation. In contrast, when the trigger cell is located at the corner or along the edge, the fewer number of neighboring cells results in greater heat absorbed by each, and therefore, a greater risk of thermal runaway propagation into the neighbors. The outcome of this trade-off most likely depends on the specific values of parameters such as cell-to-cell gap, interstitial thermal conductivity, heat rate, etc.

Numerical simulations are carried out in order to quantitatively investigate these competing considerations and determine if the corner or center location of the trigger cell is preferable to avoid thermal runaway propagation. Two simulations are carried out with the trigger cell either in the center or on the corner of a 5 by 5 array, with a cell-to-cell gap of 4 mm and interstitial thermal conductivity of  $0.02 \text{ Wm}^{-1} \text{ K}^{-1}$ . A heating rate of  $4 \times 10^5 \text{ Wm}^{-2}$  in the sleeve heater up to 400 s is considered along with Arrhenius heat generation for decomposition reactions as summarized in Table I. Under these conditions (Scenario A), Figs. 8 and 9 present temperature color-maps and plots of cell temperatures as functions of time for the two different positions of the trigger cell. These results clearly show that the case with trigger cell in the center sees thermal runaway propagation, with eventual spread to the entire battery pack. On the other hand, thermal runaway is limited only to the trigger cell when located on the corner. These results indicate that under the specific parameters values used here, the effect of closer access to external cooling plays a critical role in preventing the propagation of thermal runaway in the corner trigger cell case.

While Figs. 8 and 9 suggest a greater likelihood of propagation from a trigger cell at the center of the pack, this result is by no means universal. It may be possible that the balance between the two competing factors governing thermal runaway propagation may tilt differently in a different thermal abuse scenario. Figures 10 and 11 present results from a similar investigation of the impact of trigger cell location, but with more restricted external cooling conditions. In this case, cell-to-cell gap and interstitial thermal conductivity are the same as Figs. 8 and 9, but heating rate is  $3 \times 10^5 \text{ Wm}^{-2}$  and the

external boundaries are adiabatic. In this case (Scenario B), Figs. 10 and 11 show that thermal runaway propagation now occurs in the corner trigger cell case but not in the center trigger cell case. Clearly, reduction in the external convective heat transfer coefficient reduces the advantage of the corner trigger cell seen in Figs. 8 and 9. This makes it more likely for thermal runaway to propagate from the corner trigger cell, which shares its heat with a fewer number of neighbors than the center trigger cell, thereby leading to more temperature rise per neighbor.

**Impact of radiation and free convection heat transfer.**—The computational framework developed for simulations described above combines three non-linear thermal processes—Arrhenius heat generation, radiation and natural convection—into a single simulation. Inclusion of these non-linear processes likely makes the simulation results more accurate and realistic than if these processes were not modeled. However, the complex interaction between these non-linear processes also makes the computations challenging and increases the computation time. In order to optimize these simulations, it is of interest to determine whether any of these processes can be reasonably neglected, thereby saving on computational cost. While Arrhenius heat generation must clearly be accounted for in any thermal runaway simulation, a set of simulations are carried out to determine the impact of neglecting radiation and natural convection on the accuracy of simulation results. Both radiation and natural convection enhance the rate of heat transfer between cells, and therefore, it is important to understand whether these modes of heat transfer are sufficient to influence the propagation of thermal runaway.

In the first set of simulations, the effect of modeling radiative heat transfer is determined. For a representative set of parameter values, Figs. 12a and 12b plot temperature curves for each cell in the pack with and without radiation modeling, respectively. A comparison of these plots shows that the battery pack undergoes severe thermal runaway when radiation is modeled. On the other hand, neglecting radiation leads to a prediction of onset in the trigger cell but no propagation. This shows that radiation modeling is of critical importance, and that neglecting radiation may result in an erroneous prediction of no thermal runaway propagation, when, in fact, propagation may occur. This can, of course, be dangerous from a safety perspective.

Similarly, the effect of natural convection, which also facilitates cell-to-cell heat transfer is also characterized. Two simulations—with and without natural convection—are carried out while all other problem parameters are held constant. Natural convection is turned off by setting the value of  $\beta$  to be zero. Figure 13 compares temperature rise as a function of time for full-scale simulations with the one without natural convection. Thermal runaway is found to propagate both with and without natural convection. However, when natural convection is not modeled, a milder propagation is predicted.

For example, as shown in Fig. 13a, the neighboring cells 2 and 7 enter thermal runaway roughly 40 s and 90 s after runaway in the trigger cell when natural convection is modeled. In contrast, when natural convection is not accounted for, the reduced inter-cell heat transfer causes a delay in thermal runaway propagation, so that cells 2 and 7 now enter thermal runaway 95 s and 310 s after runaway in the trigger cell, as shown in Fig. 13b. This indicates that neglecting natural convection is also undesirable. Even though neglecting natural convection does not result in the incorrect prediction of no propagation, it still incorrectly predicts a slow propagation of thermal runaway.

### Conclusions

The onset and propagation of thermal runaway involves multiple non-linear thermal processes. It is important to develop a systematic simulation framework to account for these processes and their interactions with each other, in order to ultimately be able to accurately predict whether thermal runaway propagation will occur or not. This work shows that cell-to-cell gap and thermal conductivity of the interstitial medium both play a key role in determining the nature of thermal runaway in the battery pack. While a large value of the cell-to-cell gap may help prevent propagation, it also reduces the energy storage density of the battery pack. In different thermal abuse scenarios, both very low and very high values of thermal conductivity are found to be undesirable, with an intermediate range being the most desirable. The effect of location of the trigger cell within the pack is also investigated, and it is found that either the center or the corner location may be desirable, depending on the nature of thermal abuse. Further, results related to the effect of neglecting radiation or natural convection clearly show that these effects must be properly accounted for in order to ensure accuracy of the simulation. It is expected that the results discussed here may be helpful for practical thermal design of the battery pack, as well as for the developing practical thermal simulation tools for battery packs.

### Acknowledgments

This material is based upon work supported by CAREER Award No. CBET-1554183 from the National Science Foundation. The

authors would like to gratefully acknowledge helpful discussions with Dr. Judy Jeevarajan, Carlos Lopez, Mohammed Parhizi, Krishna Shah and Saad Azam.

### ORCID

Ankur Jain  <https://orcid.org/0000-0001-5573-0674>

### References

1. B. Diouf and R. Pode, *Renew. Energy*, **76**, 375 (2015).
2. T. Reddy (ed.), *Linden's Handbook of Batteries* (McGraw-Hill, New York, NY) 4th ed. (2010).
3. K. Shah, V. Vishwakarma, and A. Jain, *J. Electrochem. Energy Convers. Storage*, **13** (2016).
4. T. M. Bandhauer, S. Garimella, and T. F. Fuller, *J. Electrochem. Soc.*, **158**, R1 (2011).
5. R. Spotnitz and J. Franklin, *J. Power Sources*, **113**, 81 (2003).
6. I. Esho, K. Shah, and A. Jain, *Appl. Therm. Eng.*, **145**, 287 (2018).
7. R. C. Shurtz et al., *J. Electrochem. Soc.*, **166**, A2498 (2019).
8. K. Shah, D. Chalise, and A. Jain, *J. Power Sources*, **330**, 167 (2016).
9. P. Huang, H. Chen, A. Verma, Q. Wang, P. Mukherjee, and J. Sun, *J. Hazardous Mater.*, **369**, 268 (2019).
10. K. Shah and A. Jain, *Int. J. Energy Res.*, **43**, 1827 (2019).
11. G. H. Kim, A. Pesaran, and R. Spotnitz, *J. Power Sources*, **170**, 476 (2007).
12. X. Feng et al., *Appl. Energy*, **154**, 74 (2015).
13. J. Lamb, C. J. Orendorff, L. A. M. Steele, and S. W. Spangler, *J. Power Sources*, **283**, 517 (2015).
14. W. Q. Walker et al., *J. Power Sources*, **415**, 207 (2019).
15. C. F. Lopez, J. A. Jeevarajan, and P. P. Mukherjee, *J. Electrochem. Soc.*, **162**, A1905 (2015).
16. R. M. Spotnitz, J. Weaver, G. Yeduvaka, D. H. Doughty, and E. P. Roth, *J. Power Sources*, **163**, 1080 (2007).
17. R. Spotnitz and R. Muller, *Electrochem. Soc. Interface*, **21**, 57 (2012).
18. M. Chen et al., *Energies*, **8**, 490 (2015).
19. L. Torres-Castro, A. Kurzwski, J. Hewson, and J. Lamb, *J. Electrochem. Soc.*, **167**, 090515 (2020).
20. W. A. Hermann, S. I. Kahn, V. H. Mehta, and D. G. Beck, US Patent No. 8541126B2 (2013).
21. Q. Li et al., *J. Power Sources*, **429**, 80 (2019).
22. A. Prilutsky and W. A. Hermann, US Patent No. 9093726B2 (2015).
23. J. Xu, C. Lan, Y. Qiao, and Y. Ma, *Appl. Thermal Eng.*, **110**, 883 (2017).
24. M. Parhizi, M. B. Ahmed, and A. Jain, *J. Power Sources*, **370**, 27 (2017).
25. T. L. Bergman, A. S. Levine, F. P. Incropera, and D. P. Dewitt, *Fundamentals of Heat and Mass Transfer* (Wiley, New York) 8th ed. (2020).
26. T. S. Bowling, *J. Atmos. Terr. Phys.*, **56**, 539 (1994).
27. T. Walker, S. C. Xue, and G. W. Barton, *J. Heat Transfer*, **132**, 1 (2010).
28. S. J. Drake et al., *J. Power Sources*, **252**, 298 (2014).